Opto-Electronic Advances

CN 51-1781/TN ISSN (Print) 2096-4579 ISSN (Online) 2097-3993

PhyspeNet: An empirical physics-aware network for adaptive speckle reconstructive spectrometry

Junrui Liang, Min Jiang, Jun Li*, Zhongming Huang, Junhong He, Yanting Guo, Yanzhao Ke, Jun Ye, Jiangming Xu*, Jinyong Leng and Pu Zhou*

Citation: Liang JR, Jiang M, Li J, Huang ZM, He JH, Guo YT, Ke YZ, Ye J, Xu JM, Leng JY, Zhou P. PhyspeNet: An empirical physics-aware network for adaptive speckle reconstructive spectrometry. *Opto-Electron Adv* **9**, 250299 (2026).

https://doi.org/10.29026/oea.2026.250299

Received: 5 November 2025; Accepted: 9 March 2026; Published online: 3 April 2026

Related articles

Multi-prior physics-enhanced neural network enables pixel super-resolution and twin-image-free phase retrieval from single-shot hologram

Xuan Tian, Runze Li, Tong Peng et al

Opto-Electronic Advances 2024, **7**(9): 240060 doi: 10.29026/oea.2024.240060

Design, setup, and facilitation of the speckle structured illumination endoscopic system

Elizabeth Abraham, Zhaowei Liu

Opto-Electronic Science 2025, **4**(3): 240022 doi: 10.29026/oes.2025.240022

Smart photonic wristband for pulse wave monitoring

Renfei Kuang, Zhuo Wang, Lin Ma et al

Opto-Electronic Science 2024, **3**(12): 240009 doi: 10.29026/oes.2024.240009

More related articles in Opto-Electronic Journals Group website

Opto-Electronic Advances

Article
2026, Vol. , No.

Open Access

PhyspeNet: An empirical physics-aware network for adaptive speckle reconstructive spectrometry

Junrui Liang[1†], Min Jiang[2†], Jun Li[1]*, Zhongming Huang[1], Junhong He[1], Yanting Guo[1], Yanzhao Ke[1], Jun Ye[1,3,4], Jiangming Xu[1]*, Jinyong Leng[1,3,4] and Pu Zhou[1]*

Abstract: The speckle reconstructive spectrometer (RS) is revolutionizing the design paradigm of spectrometers, shifting from hardware-dominated architectures to algorithmically driven, computing-focused methodologies. However, traditional spectral reconstruction algorithms with pre-defined regularizes suffer from suboptimal adaptability, and similarly, deep learning methods struggle to handle unseen data types once deployed. Here we propose a physics-aware spectral reconstruction framework named PhyspeNet, which consists of a convolutional neural network (CNN) and an empirical physics model, facilitating adaptive reconstruction of multiple spectral types without pre-training. The inherent structural priority in the CNN architecture provides an adaptive and remarkably powerful regularization, while the embedded empirical model endows our framework with generality across various dispersive devices, even those exhibiting complex light propagation beyond the scope of analytical models. By leveraging PhyspeNet, we attain a resolving power of 7×10^5, surpassing existing spectral reconstruction neural networks trained on polychromatic data. A 700 nm operating range in the near-infrared region is also realized, which, to the best of our knowledge, stands as the widest operational bandwidth ever reported in speckle spectrometry. We believe that this work constitutes a solid step toward adaptive speckle RSs and paves the way for advances in diverse fields, including high-dimensional light field detection, biomedicine and so on.

Keywords: reconstructive spectrometer; speckle; physics-aware neural network; empirical model

DOI: 10.29026/oea.2026.250299 | CSTR: 32247.14.oea.2026.250299

Citation: Liang JR, Jiang M, Li J et al. PhyspeNet: An empirical physics-aware network for adaptive speckle reconstructive spectrometry. *Opto-Electron Adv*, 250299 (2026).

1 Introduction

In scientific research and modern industry, spectrometers stand as indispensable analytical tools with critical applications spanning environmental monitoring, biochemical analysis, laser characterization, and beyond[1−5]. Conventional spectrometers adopt hardware-centric designs that rely on bulky dispersive optics, which suffer from heavy weight, limited spectral range, and slow measurement speed[6,7]. In recent years, reconstructive spectrometers (RSs) have gained prominence by shifting the demands from optical hardware to computational reconstruction. In particular, by integrating advanced algorithms with exploitable spectral-to-spatial mapping structures, speckle-based RSs largely eliminate the need for specialized spectral response engineering[7], demonstrating significant potential for high resolution[8,9], compact size[10,11], unlimited free spectral range[6,12], and fast response[13,14]. In speckle RS systems, a light beam is injected into a disordered medium, and each wavelength generates a unique intensity pattern on the sensor, serving as a spectral "fingerprint". Spectra cannot be directly obtained from the complex features of patterns. Instead, spectra typically need to be reconstructed by solving an ill-posed linear equation system[7]. Spectral reconstruction algorithms including truncated singular value decomposition (TSVD)[15,16],

Received: 5 November 2025
Accepted: 9 March 2026
Published online: 3 April 2026

[1]College of Advanced Interdisciplinary Studies, National University of Defense Technology, Changsha 410073, China; [2]Test Center, National University of Defense Technology, Xi'an 710106, China; [3]Nanhu Laser Laboratory, National University of Defense Technology, Changsha 410073, China; [4]Hunan Provincial Key Laboratory of High Energy Laser Technology, National University of Defense Technology, Changsha 410073, China.
†These authors contributed equally to this work.
*Correspondence: J Li, E-mail: lijun_gfkd@nudt.edu.cn; JM Xu, E-mail: jmxu1988@163.com;
P Zhou, E-mail: zhoupu@nudt.edu.cn

Lasso regularization[17,18], Tikhonov regularization[19,20], and their combinations[21–23] have been applied to address this ill-posed inverse problem by adding appropriate constraints to the spectral solutions. Artificially designed regularizers impose prior knowledge or assumptions on the target spectrum (e.g., sparsity and smoothness)[24,25], which is impractical in novel scenarios where the spectral characteristics are unknown.

With the advancement of artificial intelligence (AI), supervised learning-based neural networks have been employed to solve the inverse problem of spectral reconstruction[26–28]. Such models require massive high-quality training datasets (see detailed summary in Supplementary Table S1) to learn the mapping between the incident spectrum and spectrum-encoded patterns. The performance of the trained model is highly dependent on the quality and quantity of available datasets. Some AI-driven high-resolution wavemeters utilizing accessible monochromatic datasets are limited to detecting only the central wavelength[29–34]. A further challenge arises when training a model to reconstruct multi-wavelength target spectra, as generating diverse high-resolution polychromatic datasets is rather difficult, typically requiring multiple discrete components to adjust the wavelengths or intensities of multiple monochromatic beams. Experimental polychromatic datasets reported in previous work exhibit limited diversity, containing only single-digit spectral peaks (Supplementary Section 1). Additionally, acquiring high-resolution polychromatic ground-truth values requires advanced optical elements, such as echelle gratings[35], virtual image phase arrays[36], and other devices[37,38], making the labeling work resource-intensive and costly. Supervised learning strategies further suffer from the limitation that they achieve favorable performance only when test data shares a similar distribution to the training set[39–41], thereby constraining their generalization across diverse spectral types (Supplementary Table S2). Transfer learning can alleviate this problem to some extent[8], but it still requires fine-tuning the pre-trained model on a subset of new-type data. The additional effort to collect data and fine-tune the trained models poses practical challenges across various applications.

Furthermore, pure data-driven networks function without adhering to physical laws, frequently producing outputs that appear plausible but lack reliability. In domains requiring authenticity (e.g., spectroscopic metrology), users prioritize high-confidence results with strict physical interpretability. To enforce physical consistency, untrained neural networks and structural prior[42,43] have been introduced in holography[44–47], imaging[48–51], and other fields[52,53], through minimizing the difference between measured intensities and intensities reconstructed by a physical process. Typical physics-guided neural networks rely on analytical theories, e.g., diffraction optics in homogeneous media[39,54]. However, toward an RS with high wavelength sensitivity, it is desirable to employ inhomogeneous spectral encoding media with random internal structures (e.g., scattering systems), and the accurate modeling of such media proves prohibitively complex. Consequently, deriving explicit analytical formulations to guide convergence in untrained neural networks becomes fundamentally challenging for the RSs.

In this work, we present PhyspeNet, a novel untrained spectral reconstruction framework that integrates a convolutional neural network (CNN) with an empirically derived physics model of a diffusive medium. This empirical physics model is formulated as a spectral-to-spatial transmission matrix (TM) and embedded into the framework as a differentiable module, thereby enabling seamless compatibility with the backpropagation process. In spectrum recovery, PhyspeNet takes a single observed speckle pattern as input, and then the weights and biases of the CNN are optimized to recover the correct spectrum. The empirical model-based interpretation of the spectrum should mirror the input pattern, acting as a physics constraint to guide the backpropagation. PhyspeNet eliminates reliance on the assumption of spectral types and extensive polychromatic datasets, enabling lightweight polychromatic spectral measurement without pre-training. Moreover, we demonstrate that the inherent structural prior in the CNN architecture functions as an adaptive and remarkably powerful regularizer, which further improves measurement accuracy effectively. By leveraging PhyspeNet, we attain a resolving power of 7×10^5, outperforming existing neural networks trained on polychromatic data. A 700 nm operating range in the near-infrared region is also realized, which, to the best of our knowledge, represents the widest operational bandwidth ever reported in speckle spectrometry. We believe that the proposed work marks a solid step forward in developing adaptive, high-performance speckle spectrometry and will offer insightful perspectives for a broad range of advanced optical research fields.

2 Principles

Considering the speckle RS illustrated in Fig. 1(a), unlike conventional spectrometers that employ one-to-one spectral-to-spatial mapping (where each sensor element directly measures a discrete spectral band), speckle RSs utilize a complex spectral-to-spatial encoding and reverse decoding mechanism. Specifically, the full spectral information S is randomly scrambled in the spatial domain, leading to a pattern I sampled by a sensor array. This pattern I is subsequently decoded through algorithms to recover S. Before constructing the PhyspeNet, it is essential to introduce the spectrum decoding principles of typical data-driven neural networks. A vast array of labeled data (S_k, I_k), $k = 1, 2,\cdots, K$, is collected to form a dataset $D = \{(S_k, I_\mathrm{k}), k = 1, 2,\cdots, K\}$, and the neural network learns the mapping relationship A between these data pairs by solving the following:

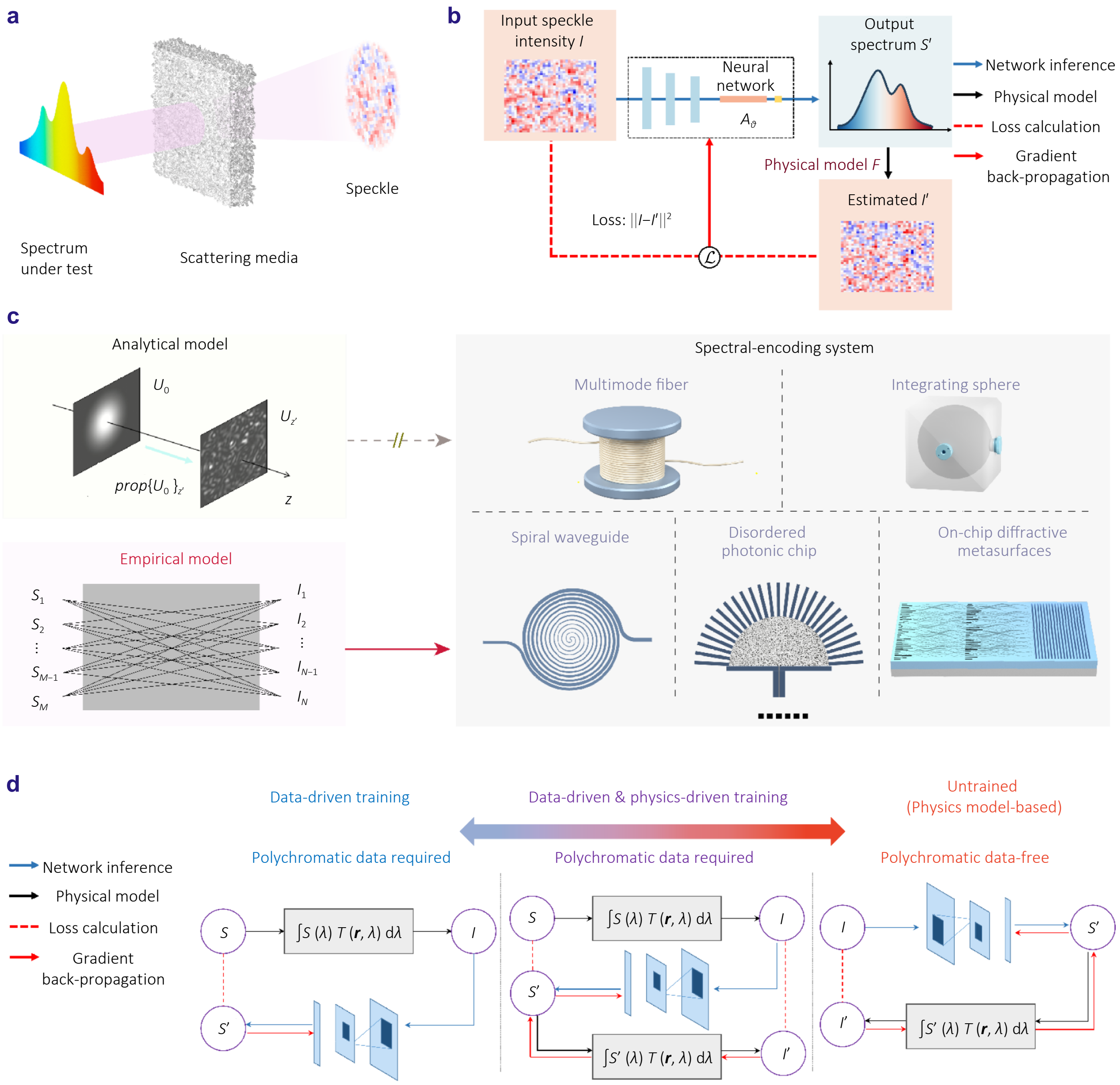

Fig. 1 | Principles of the speckle RS via physics-aware neural network. (a) Working principle of the speckle-based RS. (b) Pre-training-free pipeline of PhyspeNet for spectral reconstruction. (c) Empirical models are superior to analytical models for characterizing the physical propagation process in spectral-encoding systems. The right panel displays several representative spectral encoding systems where light undergoes disordered propagation[9,23,55–57]. Only partial spectral encoding systems are shown, while PhyspeNet is applicable to more systems wherever the TM can be calibrated. (d) Diagrams of PhyspeNet and other existing neural networks for spectral reconstruction.

$$A_{\theta^*} = \underset{\theta \in \Theta}{\operatorname{argmin}} \|A_\theta(I_k) - S_k\|_2^2, \quad \forall\,(S_k, I_k) \in D\,, \tag{1}$$

where A_θ represents the mapping function of the neural network, characterized by a set of weights and biases θ belonging to the parameter space Θ, $\|\ \|_2$ represents the L2-norm. Once the neural network training is complete, the corresponding spectrum of a newly observed speckle pattern can be obtained by $S' = A_{\theta^*}(I)$. In RSs, the size K of the training set can range from a few thousand to tens of thousands. Gathering such an extensive collection of speckle patterns I_k and their corresponding ground-truth spectra S_k experimentally is difficult (see summary in Supplementary Section 1). Moreover, the learned mapping function can only generalize effectively to spectra that share distributions similar to those of the training set.

Physical models can be integrated as constraints into a purely data-driven neural network to improve the generalizability of the spectral reconstruction. Here, we call this a data-and-physics dual-driven network (DDNet), and the mapping relationship A can be obtained by solving the following:

$$A_{\theta^*} = \underset{\theta\in\Theta}{\operatorname{argmin}} \|A_\theta(I_k) - S_k)\|_2^2 + \|F(A_\theta(I_k)) - I_k)\|_2^2, \quad \forall (S_k, I_k) \in D \,, \tag{2}$$

where $F(\cdot)$ is defined through the forward physical model, bridging the predicted spectra and observed speckle pattern. In current physics-driven neural networks, the $F(\cdot)$ is typically derived from analytical theories that can explain the complete system evolution. However, for typical speckle-based RSs[9,23,55–57] as illustrated in Fig. 1(c), light undergoes either strong scattering, complex interference and energy coupling, or random diffraction within the spectral-encoding media. Analytical approaches fail to accurately model the underlying processes and are thus inapplicable to such black-box systems. By contrast, the TM model avoids detailed simulation of internal optical dynamics, concentrating only on the multiple input-output relationships. Furthermore, as the TM is directly measured from realistic system responses, it inherently bypasses limitations of analytical theory, such as non-ideal material properties, inaccurate optical path length estimations, and so on. Thus, it serves as an ideal forward model for opaque speckle RS systems. As a result, the input-output relationship can be simplified as follows:

$$\begin{aligned} I(\boldsymbol{r}) &= F(\boldsymbol{r}, S) \\ &= \int S(\lambda) P(\boldsymbol{r}, \lambda) R(\lambda) \mathrm{d}\lambda \\ &= \int S(\lambda) T(\boldsymbol{r}, \lambda) \mathrm{d}\lambda \,, \end{aligned} \tag{3}$$

where $P(\boldsymbol{r}, \lambda) \in \mathbb{R}^{M\times N}$ is the position-dependent, spectral-to-spatial encoding function. $\boldsymbol{r}$ denotes the spatial position, and λ denotes the wavelength. M represents the spectral channel number of interest, and N represents the spatial channel number. $R(\lambda) \in \mathbb{R}^{N\times N}$ refers to the spectral-dependent sampling function of the sensor array. $T(\boldsymbol{r}, \lambda) \in \mathbb{R}^{M\times N}$ denotes the total TM characterizing both $P(\boldsymbol{r}, \lambda)$ and $R(\lambda)$, which is measured in the calibration procedure.

By utilizing the empirical $F(\cdot)$, the reconstructed speckle can be calculated from the spectrum predicted by DDNet. The difference between reconstructed and actual input speckles is incorporated into the objective function to guide DDNet training and prevent it from over-fitting. However, Eq. (2) shows DDNet still requires massive labeled spectral-speckle pairs, without addressing the challenge associated with polychromatic data acquisition.

In this study, we argue that instead of using a physical model as an additional constraint to guide network training, directly combining them in an untrained framework offers a more efficient methodology that leverages the structural prior intrinsic to a CNN. Here, we propose PhyspeNet, a novel spectral reconstruction model featuring a polychromatic data-free design. Figure 1(b) illustrates its workflow chart. PhyspeNet is based on an elegant CNN (see details in Method and Supplementary Section 3), and receives a captured speckle pattern I as input. The output of the CNN is considered the estimated spectrum S', which is subsequently fed into the physical model F to produce I'. The mean square error (MSE) between the I and I' is computed as the loss value to tune the parameters θ of the neural network:

$$A_{\theta^*} = \underset{\theta\in\Theta}{\operatorname{argmin}} \|F(A_\theta(I)) - I\|_2^2 \,. \tag{4}$$

Figure 1(d) also presents a comparative schematic illustrating the principles of our proposed PhyspeNet alongside existing neural network-based methods for spectral reconstruction (see details in Supplementary Section 4). It is important to understand that our method is not merely a straightforward alteration by eliminating S from Eqs. (1) and (2); rather, it reshapes the entire problem-solving framework. Firstly, the training procedure is removed, and an extensive labeled dataset is not required. Secondly, unlike the parameters that are fixed after training in Eq. (1) and (2), those of PhyspeNet are updated continuously during the spectrum reconstruction process. Each newly observed speckle is processed by the network, which starts with fixed random weights. Then the optimization is performed by repeatedly predicting S and updating the weights via back-propagation, until the parameters are gradually fitted to satisfy Eq. (4). Once the optimization is complete, the derived mapping function A_θ can be employed to reconstruct the spectra: $S' = A_{\theta^*}(I)$.

Finally, compared to the pure physical model-based optimization methods, it is unnecessary for PhyspeNet to elaborately design the regularization terms. In practice, to mitigate the ill-posed nature of spectral reconstruction, conventional methods commonly solve the following problem:

$$S' = \underset{S}{\operatorname{argmin}} \|F(S) - I\|_2^2 + \Gamma(S) \,, \tag{5}$$

where $\Gamma(S)$ is a regularizer. The selection of $\Gamma(S)$, which typically requires a generic prior or an assumption on spectra, is difficult and remains an active area in the field of RSs. For instance, a simple regularizer $\Gamma(S)$ could be the L1 norm of the spectrum, which promotes sparse solutions. However, once selected, these regularizers are relatively rigid and cannot flexibly adapt to a variety of spectral types. In this study, we replace conventional regularization methods with the structural prior of a neural network architecture that possesses inherent regularization capabilities (Supplementary Section 11). This regularization effect has been demonstrated to stem from the inherent spectral bias of CNNs[58–60], which typically exhibits strong resistance to noise while preserving low resistance to signals[42].

3 Results

3.1 Polychromatic-data-free reconstruction with high generalization

We first compare the generalization performance of the PhyspeNet against other spectrum reconstruction models that require training by using synthesized spectra with distinct features (I. broadband continuous, II. narrowband continuous, III. narrowband sharp, and IV. broadband sharp). The synthesized spectra are generated by summing experimentally recorded intensities corresponding to different monochromatic lights with user-specified weights. Details of the experimental apparatus are shown in the Method section and Supplementary Section 5. Among the concerned spectral types, Spectral Type I comprises the training set for pure data-driven neural network and DDNet (see dataset generation strategy in Supplementary Section 6), as it can be easily produced by off-the-shelf products[28,61]. In contrast to Spectral Type I, the large-scale preparation of the latter three spectrum types entails specialized equipment, including devices with narrowband or sharp filtering edges and tunable capabilities. During the model test, we incorporate all types of spectra as detection targets. Consequently, our testing protocol mimics a real scene where a network trained on a single spectral distribution is employed to identify unknown spectra from various distributions. In particular, a Lorentz spectrum with full width at half maxima (FWHM) linewidth of 0.25 nm, a Lorentz spectrum with FWHM linewidth of 0.025 nm, a random multi-line spectrum with relative sparsity ratio (RSR) of 3%, and a rectangle spectrum with a width of 0.5 nm are selected for intuitive illustration here. The RSR is defined as the ratio of non-zero spectral channels to the total calibrated spectral channels[24]. Notably, the 0.25 nm FWHM linewidth Lorentz spectrum for the test here is absent from the training dataset; instead, it features a data distribution analogous to that of Spectral Type I.

Figure 2(a) presents the observed speckle patterns associated with four representative spectra. The narrowband spectra depicted in the second and third columns are characterized by speckles with diminished intensity, heightened contrast, and a richer array of spatial features compared to the broadband spectra in the first and fourth columns. This phenomenon arises because the M simultaneous wavelengths add in intensity[26,62], leading to a contrast reduction of ~$M^{1/2}$ times the speckle's intensity for a single wavelength[25,63]. Consequently, some spatial features vanish or become homogenized. The reconstruction accuracy is most susceptible to degradation when the speckle contrast drops below the measurement noise level, which constrains the reconstruction performance for broadband spectra. The intensity probability density function (PDF) distributions of the spectrum-dependent speckle are depicted in Fig. 2(b). The intensity PDFs of narrowband speckles exhibit a distribution that closely aligns with a negative exponential envelope, a characteristic that is particularly pronounced in images with high contrast. Broadband speckle intensity distributions tend to be more uniform, with PDFs adhering closely to a Gaussian envelope. This alignment with the Gaussian distribution is anticipated based on the central limit theorem[64]. In Fig. 2(c), we further visualize the distribution of four distinct spectral speckles in the feature space derived from principal component analysis (PCA). We clearly distinguish between the speckle patterns associated with broadband spectra (blue and purple circles) and those corresponding to narrowband spectra (red and yellow circles). However, the separation of speckle patterns related to continuous and sharp spectra varies. As for broadband speckles, the features of continuous (blue circles) and sharp (purple circles) spectra are not significantly distinguishable. On the contrary, for narrowband speckles, there is a distinct separation between continuous (red circles) and sharp (yellow circles) spectra. Figure 2(d–f) display the reconstruction results for various spectra using a pure data-driven neural network (yellow lines), DDNet (blue lines), and PhyspeNet (red lines). In this work, we employ the relative L2-norm error (μ) to assess the accuracy of spectrum reconstruction (see Method), a metric widely recognized and adopted in this field[1,22]. Particularly, a relative L2-norm error below 0.1 is typically regarded as a stringent criterion that signifies high accuracy in spectral reconstruction[18,22,65,66]. As depicted in the first column of Fig. 2(d–f), the reconstruction results from all three models have met this specified standard, indicating a satisfactory level of internal generalization to new samples of the same type as those in the training dataset. The spectral reconstruction accuracy of the trained networks is marginally higher, with DDNet scoring the lowest relative error values. This superior performance can be attributed to incorporating additional physical prior constraints within DDNet. When blindly tested on unseen Spectral Type II, III, and IV, PhyspeNet achieves better external generalization than trained models using the same architecture. For Spectral Type II, the trained networks effectively identify the central peak region; however, the recovered intensity values are inaccurate. For Spectral Type III, the trained networks completely fail to reconstruct the narrowband multi-lines. Instead, the outcomes align with the shape of the broadband continua. For Spectral Type IV, the pure data-driven approach and DDNet can largely recover the intensity and position of the non-zero spectral components. However, these methods struggle to infer the steep cut-off edge, tending to derive gradually rising and falling gradient edges. Their relative reconstruction errors are 0.2388 and 0.2116, respectively. In stark contrast, PhyspeNet achieves a significantly lower relative error of 0.0312, demonstrating approximately seven-fold greater accuracy than the trained networks. Furthermore, we conduct additional spectral reconstruction experiments to validate this superiority (see Supplementary Section 7),

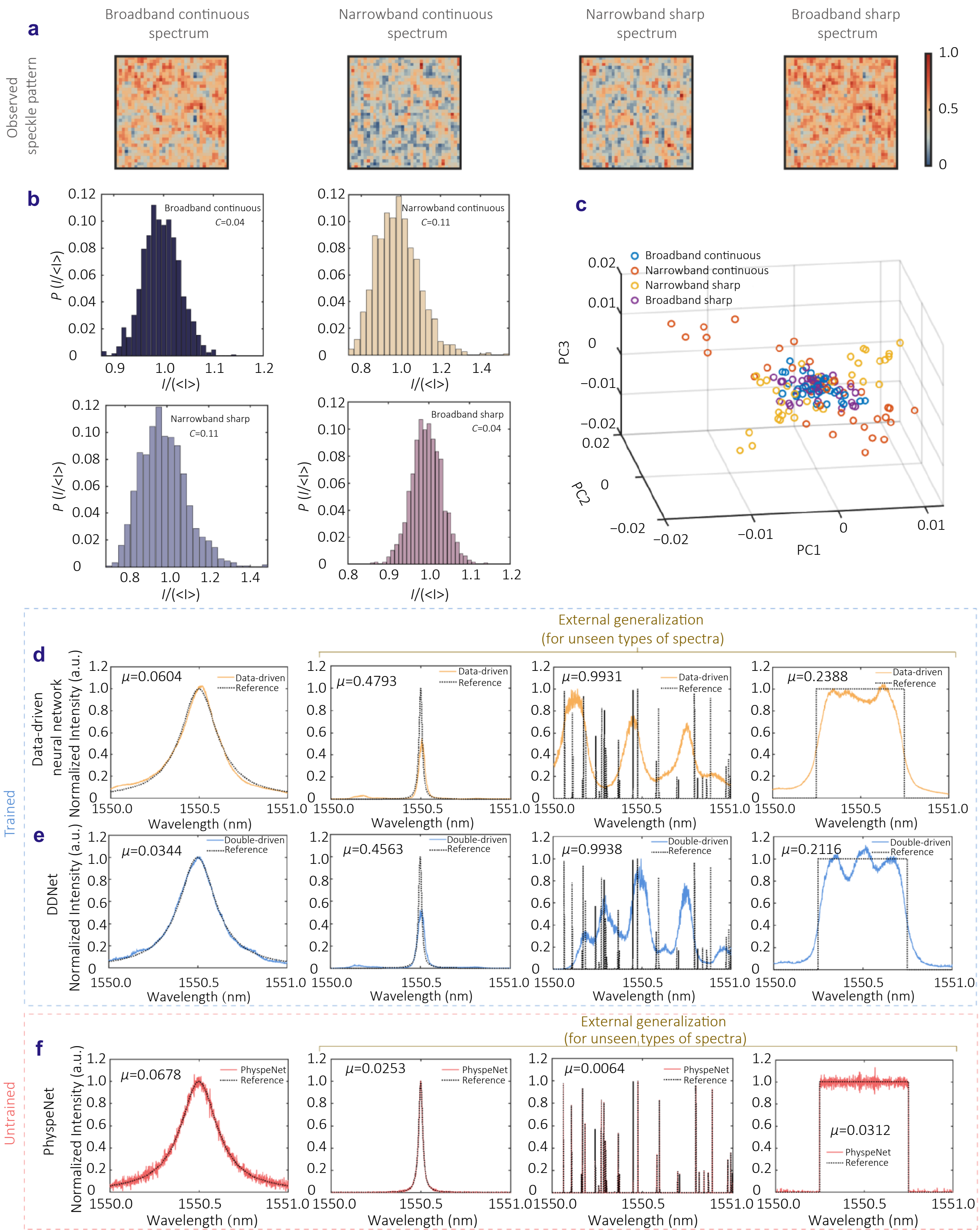

Fig. 2 | Analysis of the spectrum-dependent speckles and comparison with existing neural network models that need training for synthesized spectrum recovery. (a) Observed speckle patterns corresponding to broadband continuous, narrowband continuous, narrowband sharp, and broadband sharp spectra. (b) The intensity probability density function distribution of the speckle patterns corresponding to four spectrum types, with their intensity contrast marked. (c) Visualization of the feature space. Discernible distribution is exhibited between broadband (blue and purple circles) and narrowband signals (red and yellow circles), while there are varying degrees of differentiation among the continuous (blue and red circles) and sharp (purple and yellow circles) signals. PC: principal component. Synthesized spectrum reconstructed by the (d) pure data-driven neural network (yellow lines), (e) DDNet (blue lines), and (f) PhyspeNet (red lines).

including Spectra I with changing FWHM linewidths, Spectra II with shifts in center wavelength position, Spectra III with variations in RSRs, and Spectra IV with alterations in bandwidth. In comparison to the purely data-driven network and DDNet, PhyspeNet achieves a reduction in average reconstruction errors for the four spectral types of 79.50% and 77.83%, respectively. In summary, our results reveal that the untrained PhyspeNet model shows high reconstruction fidelity for both internal and external generalization.

3.2 Adaptive reconstruction

In addition to its generalization advantage, another benefit of PhyspeNet lies in its utilization of the structural prior provided by the neural network[42]. In this section, we compare PhyspeNet with several well-known spectral reconstruction algorithms, including Lasso regularization, Tikhonov regularization, and TSVD. Particularly, the Lasso regularization aims to minimize the $\|I-F(S)\|_2^2+\gamma\|S\|_1$, where $\|\ \|_1$ represents the L1-norm. Lasso regularization encourages to produce solutions with a small number of non-zero coefficients. In contrast, the Tikhonov regularization seeks to minimize $\|I-F(S)\|_2^2+\gamma\|S\|_2^2$. The regularization parameter γ for Lasso and Tikhonov can typically be selected through generalized cross validation (GCV) to accommodate different types of spectra[7]. In addition, TSVD is an effective noise suppression technique that enhances the stability and accuracy of spectral reconstruction. This method operates by preserving the primary features in the data while eliminating components associated with smaller singular values, often indicative of noise. Like the coefficient γ in Lasso and Tikhonov regularization, selecting the cut-off threshold in TSVD largely influences the reconstruction quality[15]. Figure 3(a) illustrates that when these classical methods are used to reconstruct different synthesized spectra (without loss of generality, we have chosen Lorentzian spectra with varying FWHM linewidths), the selection of parameters is case-sensitive to achieve optimal reconstruction accuracy. As the FWHM linewidth increases, the superposition of experimental noise leads to optimal reconstruction effects occurring at higher singular value cut-off thresholds and larger L2 regularization parameters (see the left and right columns in Fig. 3(a)). Conversely, an increase in non-zero wavelength components requires a lesser degree of L1 regularization penalty (see the middle column in Fig. 3(a)). By contrast, the proposed PhyspeNet focuses solely on the $\|I-F(S)\|_2^2$ during its optimization and no extra hyperparameters need to be tuned.

Figure 3(b–e) shows the reconstructed synthesized spectra I–IV by PhyspeNet and three representative classical algorithms. In contrast to the aforementioned neural network-based methods, classical approaches do not encounter issues related to domain shifts and are universally applicable across various types of spectral reconstructions. Compared to the smooth optical spectral curve obtained through neural network inference (see Fig. 2), the spectra reconstructed by traditional methods contain more high-frequency artifacts. Our proposed PhyspeNet retains the universality of physics-based retrieval while leveraging the regularization of the neural network. As shown in Fig. 3(b–e), the spectra recovered by PhyspeNet has fewer oscillations and demonstrates the lowest relative error values. We utilize the spectral samples from the previous section to validate the superior accuracy of PhyspeNet. More analyses are provided in Supplementary Section 8. Compared to TSVD, Lasso regularization, and Tikhonov regularization, PhyspeNet reduces the average reconstruction errors for the four spectral types by 51.77%, 84.58%, and 40.14%, respectively.

In addition to the single regularizer approach, combined regularizers can also be adopted for spectral reconstruction. However, in the absence of prior information on the incident spectrum, it is challenging to identify the optimal set of regularizers to combine. An inappropriate selection of regularizer combinations or their relative weights will significantly degrade the spectral reconstruction accuracy for specific spectral types. Moreover, the combination of multiple regularization terms leads to an exponential expansion of the search space for optimal weight tuning[67]. Our results further demonstrate that PhyspeNet outperforms composite regularization methods (see Supplementary Section 9). A comparison between PhyspeNet and non-regularized methods is also presented in Supplementary Section 10.

3.3 Practical applications of the PhyspeNet-based RS

We then apply the speckle RS based on PhyspeNet to measure various light sources. We first evaluate the performance of our RS in 1525–1565 nm using an integrating sphere (see Method). A series of single-peak spectra spanning over this range can be effectively reconstructed, as depicted in Fig. 4(a). The average spectral reconstruction error is as low as 0.0900, with an average reconstructed peak signal-to-noise ratio (PSNR) of 51.50 dB (see definition of PSNR in Method). To assess the resolution of our system, we generate and measure a dichromatic beam with a 2 pm wavelength separation using the method described in ref.[68] (Fig. 4(b)). PhyspeNet can clearly distinguish between the two close wavelengths, yielding a relative error of 0.1090 and a PSNR of 31.45 dB for the spectral reconstruction. When measuring single peaks with a fine step of 1 pm, PhyspeNet can accurately recover their respective central wavelength positions, as illustrated in the inset of Fig. 4(b). Higher resolution is constrained by the minimum stepping interval of the calibration laser. Similarly, we undertake a triple-peak detection (displayed in Fig. 4(c)), demonstrating a relative error of 0.1943 and a spectral reconstruction PSNR of 24.00 dB. In addition to demonstrating ultra-fine spectral

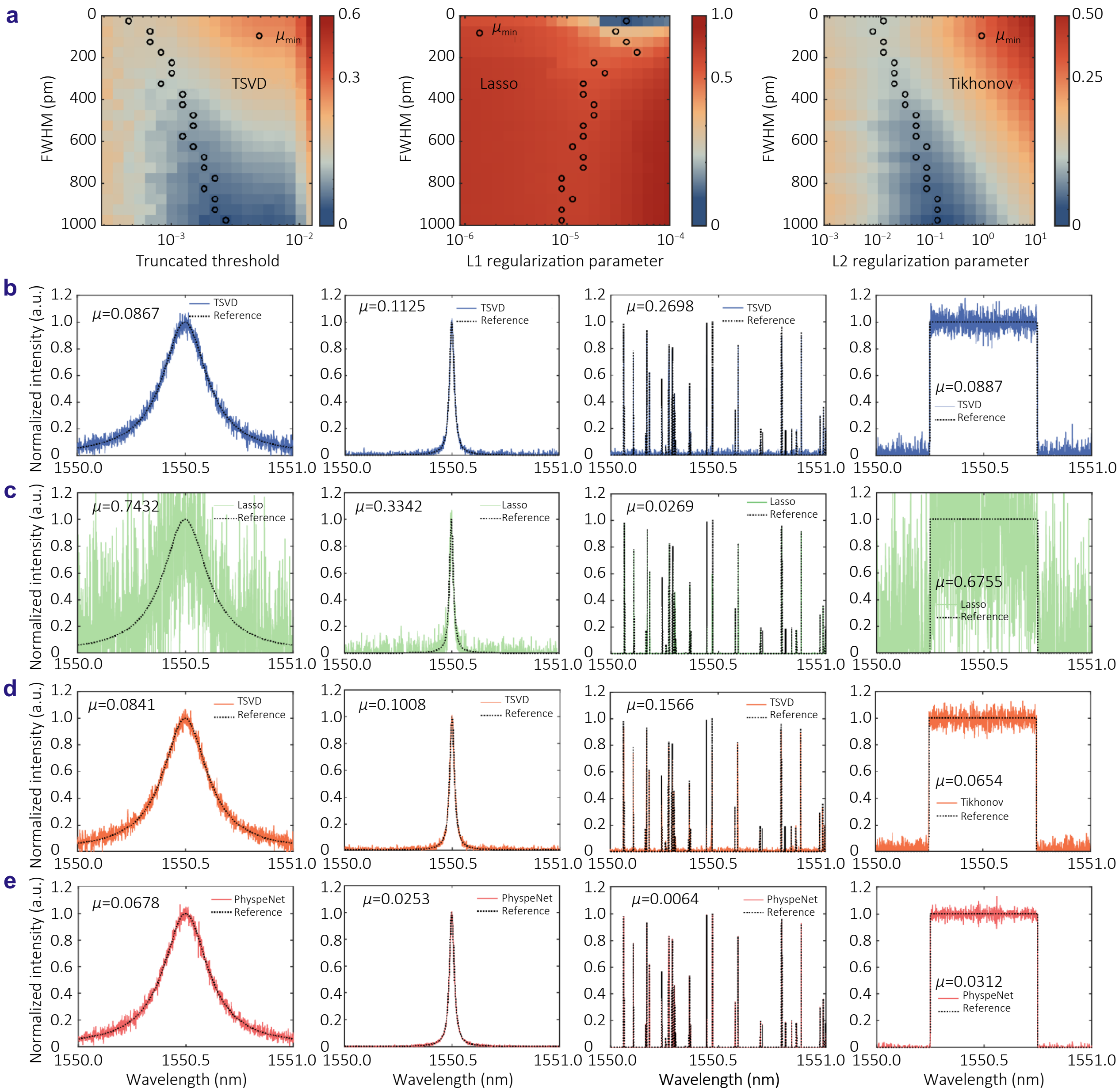

Fig. 3 | Synthesized spectral reconstruction comparison of PhyspeNet, TSVD, Lasso regularization, and Tikhonov regularization. (a) TSVD (left), Lasso regularization (middle), and Tikhonov regularization (right) methods exhibit parameter sensitivity in achieving optimal reconstruction quality for different spectral samples. Pseudocolor represents the reconstruction error under the current target spectrum and regularization parameter settings. The color bar is on a logarithmic scale. Black circles denote the points with the lowest reconstruction error. Spectrum reconstructed by the (b) TSVD (dark blue lines), (c) Lasso regularization (light green lines), (d) Tikhonov regularization (orange lines), and (e) PhyspeNet (red lines).

reconstruction using an integrating sphere, the versatility of PhyspeNet is validated on a multimode fiber configuration (see Method). As depicted in Fig. 4(d), we reconstruct the transmitted spectra of a tunable narrowband filter. Accurate spectral reconstruction across the 1000–1700 nm wavelength range (primarily limited by the spectral response of the detector) is achieved, with an average relative error of 0.2669 and PSNR of 38.74 dB. To our knowledge, this represents the largest operational bandwidth reported to date for speckle-based spectrometry. We further use PhyspeNet to characterize both a broadband spectral filter (7 nm FWHM bandwidth) and an amplified spontaneous emission (ASE) source (41 nm FWHM bandwidth), with the results showing good agreement with those measured by a commercial optical spectrum analyzer, as shown in Fig. 4(e1, e2). More comparison between PhyspeNet and other spectral reconstruction methods on practical data is provided in Supplementary Section 12. Figure 4(f) shows the observed *I* and the

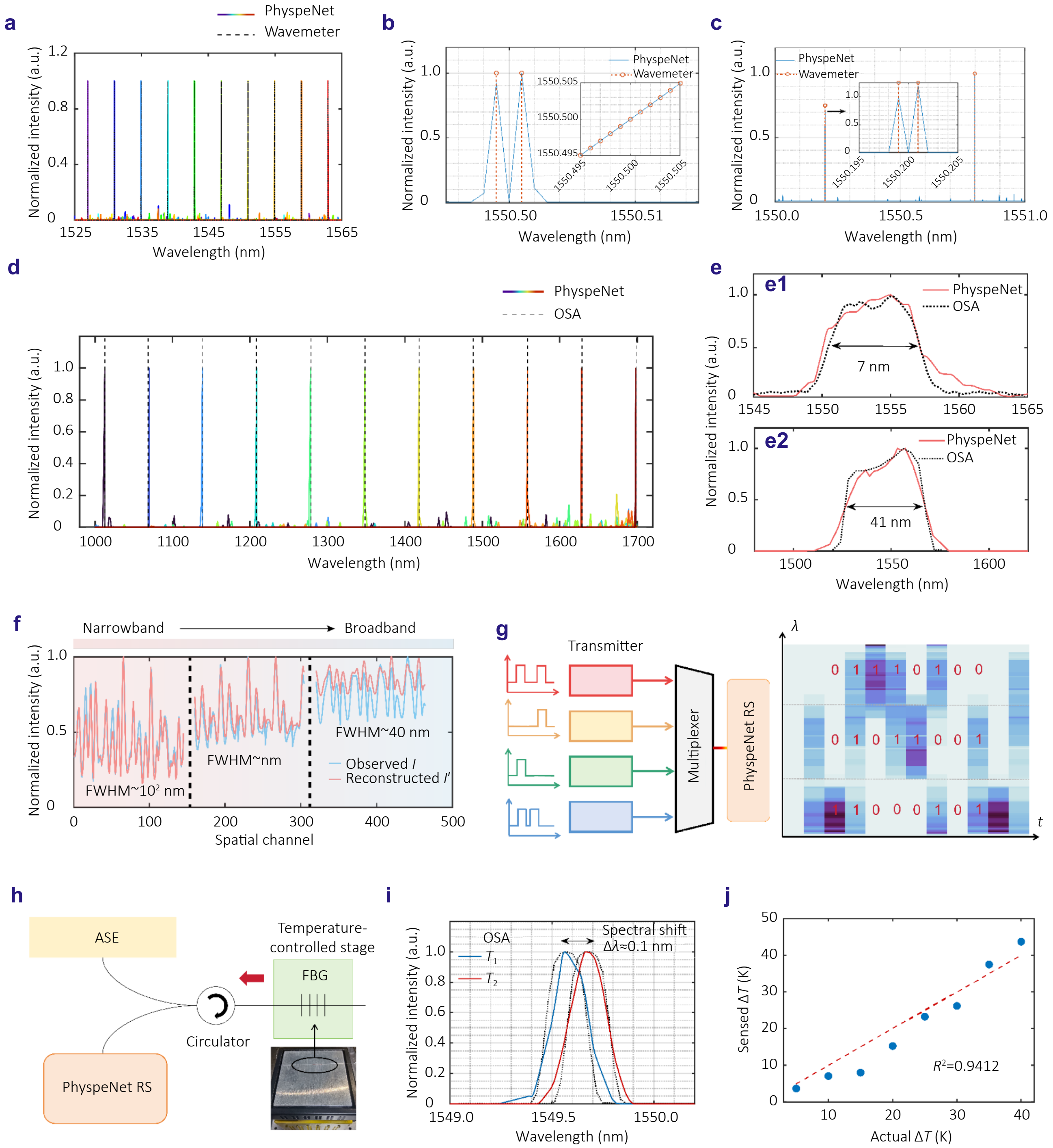

Fig. 4 | Application of the PhyspeNet empowered speckle RS on light source testing. (a) Reconstructed spectra for tuning wavelengths within 1525–1565 nm. (b) Reconstructed spectrum for dual spectral lines separated by 2 pm. (c) Reconstructed spectrum for triple wavelengths, with an interval of 2 pm between two of them. (d) Reconstructed spectrum for probe signals spanning across 1000–1700 nm. (e) (e1) Reconstructed spectrum for a probe signal with a 7 nm FWHM bandwidth. (e2) Reconstructed spectrum for an ASE source with a 41 nm FWHM bandwidth. (f) Observed and reconstructed intensity distribution corresponding to different kinds of spectra. (g) Diagram of the WDM optical communication system employing the PhyspeNet-based RS. The transmitter combines independently modulated light sources. At the receiver, our RS demultiplexes the three-waveband WDM signals and decodes the original binary data streams. (h) Schematic of the fiber sensing experimental setup deploying the PhyspeNet-based RS. The inset shows the FBG sensor mounted on the temperature-controlled stage. (i) PhyspeNet resolves spectral shifts as small as 0.1 nm. (j) Temperature sensing results obtained with the PhyspeNet-based RS system.

reconstructed I' for the different spectral types, including narrowband single-frequency light (FWHM ~0.04 pm), conventional filter-transmitted light (FWHM ~nm level), and broadband ASE light (FWHM ~tens of nm). As the spectral bandwidth increases, the contrast of the speckle grain in observed I gradually decreases, while the size of the speckle grain increases. As a result, the computational algorithm struggles to accurately reconstruct the subtle dips in the speckle grain (see the blue background area in Fig. 4(f)). To further improve reconstruction accuracy, more attention should be paid to the fine structural details of the valley features within the speckle intensity pattern.

The reliable performance of the PhyspeNet enables applications in wavelength-division multiplexing (WDM) systems. We employ multiple independently modulated light sources at distinct wavelengths (1535, 1545, and 1555 nm) as transmitters, coupling them into our RS via a beam combiner, and using PhyspeNet to retrieve the original modulation information (see Fig. 4(g)). The PhyspeNet achieves high-fidelity of spectral intensity and central wavelengths. These proficiencies establish the PhyspeNet-based RS as a viable decoder for optical WDM networks. Furthermore, we demonstrate the integration of our RS with a fiber Bragg grating (FBG) sensor for environmental monitoring. FBGs generate narrowband reflection spectra that shift in response to temperature or stress variations, making them ideal for long-term structural health monitoring in civil engineering[69]. Standard FBG interrogation requires benchtop spectrometers for spectral shift detection. Our system offers a compact solution. As illustrated in Fig. 4(h), our experimental setup consists of an ASE source illuminating an FBG (0.1 nm linewidth) mounted on a temperature-controlled stage. The reflected signal is routed through a circulator to our RS for spectral detection. When temperature variations are applied to the FBG, our system accurately resolves the resulting spectral shifts, achieving a detection sensitivity of 0.1 nm (see Fig. 4(i)). We then demonstrate temperature sensing over a 40 K range as a proof-of-concept, with experimental results agreeing with actual values. The sensing quality is quantified using the coefficient of determination (R^2), calculated as: $R^2 = 1 - \frac{\sum_i (y_i - \hat{y}_i)^2}{\sum_i (y_i - \bar{y}_i)^2}$,where y_1, $\hat{y}_i$, and $\bar{y}_i$ represent the actual and sensed temperature shift, and mean temperature shift values, respectively. As shown in Fig. 4(j), PhyspeNet achieves an R^2 of 0.9412, confirming exceptional sensing capacity.

4 Discussion

We have introduced an innovative spectral reconstruction framework based on a physics-aware neural network named PhyspeNet. By integrating the CNN with an empirical TM that faithfully represents actual system responses (see Supplementary Section 13 and Section 14 for reconstruction stability and tolerance to calibration error), PhyspeNet can be applied to various RS architectures that analytical theories fail to characterize. When using PhyspeNet for spectrum reconstruction, the loss function for updating the network parameters is calculated as the difference between the observed intensity pattern and the one reconstructed by the empirical TM model. This physics-aware loss function surpasses traditional loss functions (typically calculated using the estimated and labeled spectra) commonly used in supervised learning. The supervised learning establishes a mapping function based on the statistical properties of a substantial training dataset, which are encoded in the network's weights. When applying these same weights to test data, errors are likely to occur, leading to distortion in the reconstructed spectra, especially when the test samples differ significantly from those in the training set regarding their statistical characteristics. PhyspeNet does not derive a mapping function from the training data statistics; instead, it simultaneously leverages the network's structural prior and the universality provided by the empirical physics model. Thus, PhyspeNet will be meticulously optimized for each input, demonstrating an enhanced capacity to generalize across unseen data distributions as opposed to supervised models.

To emphasize the superiority of PhyspeNet, we compare its spectral resolving power and operating wavelength range with the state-of-the-art RSs based on artificial neural networks[21,27,28,70–78] in Fig. 5(a). This comparison highlights a critical challenge for most supervised learning-based RSs: simultaneously achieving both large operational bandwidths and high resolution requires neural networks to regress numerous spectral channels while distinguishing small wavelength changes. In our context, "spectrometers" refers to those that permit the reconstruction of multiple wavelengths instead of merely a single wavelength (more technically termed wavemeters). As shown in Fig. 5(a), most reported studies focus on the visible-light region, while investigations on the near-infrared band predominantly rely on simulated datasets (see Supplementary Section 1). Studies using simulated and experimental polychromatic data are marked by hollow squares and solid circles, respectively. To our knowledge, using fully experimental polychromatic datasets remains exceptionally rare in the extensive community of RSs — a testament to the challenges of polychromatic data generation and labeling. Our approach circumvents this bottleneck by eliminating the need for polychromatic data, while demonstrating effective spectral reconstruction across 700 nm in the near-infrared region. In terms of spectral resolving powers (defined as the ratio of the central wavelength to the spectral resolution), all values considered here were validated through dual-peak testing following the Rayleigh criterion[22]. As is evident from Fig. 5(a), our method achieves a spectral resolving power of 7×10^5, higher than other comparable neural network-based RSs.

While one study[27] in Fig. 5(a) also shows high spectral resolving power, its network outputs only ~150 wavelength channels per single measurement (see Fig. 5(b)). Figure 5(b) further compares the reported single-measurement channel capacity of data-driven networks. It is well known that each wavelength-channel-dependent intensity profile constitutes a basis state. For polychromatic light measurement, as the number of potential wavelength channels involved increases, the neural network must project the observed polychromatic intensity profile onto a larger combinatorial space of these basis states. This typically demands larger training datasets to cover possible combinations. PhyspeNet breaks this inherent trade-off by operating without pre-training, enabling ~1,000 spectral channel reconstructions independent of training data volume. Increasing the number of spectral channels will be the focus of our future work.

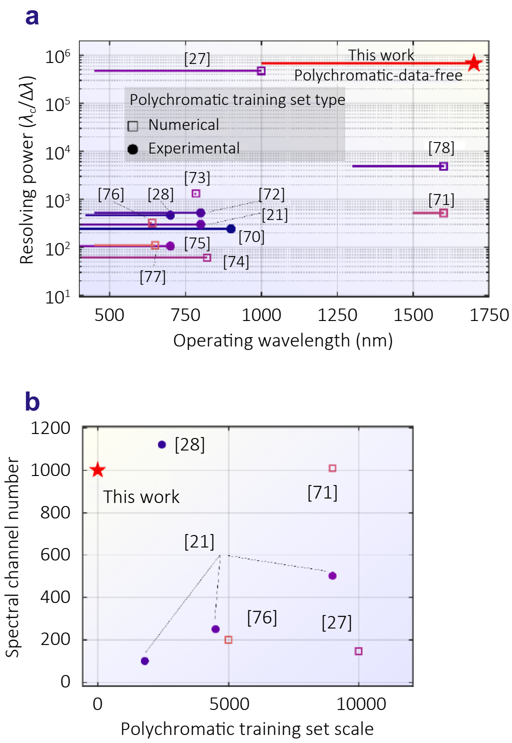

Fig. 5 | Comparison with state-of-the-art RSs based on artificial neural networks. Comparison regarding the (a) resolving power and operating wavelength, (b) reconstructed spectral channel number and polychromatic training dataset scale. λ_c represents the operational central wavelength, and $\Delta\lambda$ represents the spectral resolution. The hollow squares represent schemes based on simulative polychromatic training sets, while the solid circles represent schemes based on experimental polychromatic training sets.

PhyspeNet also saves dozens of hours that would be spent on training (see Supplementary Section 4), which is crucial for the rapid deployment and operation of RS systems while ensuring strong generalization capability. However, due to its iterative optimization process, it requires a single-inference time of approximately 1 minute. Though it still superior to reported non-neural-network methods[2,79] of comparable computational scale (>5 minutes), it remains slower compared to pre-trained networks (~1 ms). This thus reflects a trade-off between inference speed and generalization performance. In the future, spectral inference speed can be improved by reducing spatial channel sampling[14,29], exploring advanced optimization approaches[43], and designing lightweight network architectures[80,81] tailored specifically for spectral reconstruction.

Beyond surpassing existing AI-based spectral reconstruction methods, PhyspeNet outperforms classical non-AI methods, which use explicit regularizers based on spectral priors. However, there is often a lack of prior information regarding the distribution of the spectra to be measured. Selecting an elegant regularizer for diverse spectra types and effectively applying it to enhance recovery performance remains a challenge. Even after choosing the appropriate regularizers, accurate reconstruction further needs adjusting the regularization hyperparameters carefully. To achieve higher computational adaptability, PhyspeNet utilizes a network architecture to enforce structural priors, eliminating the need for assumptions about unknown spectra and the trial-and-error of regularization terms.

Last but not least, although we have demonstrated PhyspeNet's effectiveness only on speckle-based RSs, the framework can extend to another RS strategy that is based on spectral response engineering[7,19,82–84], where the random spectral response is difficult to model analytically and is typically represented in an empirical matrix form. Moreover, thanks to its flexible scalability, the PhyspeNet might lend itself to a vast range of application, such as high-dimensional light field detection[85], biomedicine[82], and so on[86].

5 Method

5.1 Experimental setup

Before utilizing the spectrometer, it is essential to calibrate the relationship between wavelength and spatial speckle to establish an empirical TM of the scattering medium. At this stage, a tunable laser (tuning range: 1520–1567 nm, FWHM linewidth: 0.04 pm) is used to vary wavelengths in a moderate range. A supercontinuum light source equipped with an acousto-optic tunable filter is used to change the wavelength over a wide range of 1000–1700 nm. The light beam enters the scattering medium via a polarizer, which aims to maintain the polarization state of the input light, ensuring that a specific wavelength consistently produces the identical speckle pattern. The two most commonly used spectral-encoding scattering mediums are adopted to verify the universality of the PhyspeNet framework. One is an integrating sphere (diameter = 2.5 cm, output port diameter = 3 mm). Its internal surface material is barium sulfate ($BaSO_4$), selected for its high reflectance (> 95%), excellent chemical stability, and spectral neutrality. Without loss of generality, the integrating sphere-encoded speckle patterns are used for synthetic spectrum reconstruction to compare PhyspeNet with other algorithms. Another scatterer is a two-meter-long multimode fiber (core diameter = 105 μm, NA = 0.22). The speckle pattern produced by the scattering medium is imaged on the camera without the use of lenses. The camera features a pixel size of 20 μm × 20 μm, a resolution of 320 × 256 pixels, and a 14-bit grayscale depth. The laser and camera are synchronized using a homemade control program, which allows us to align the speckle pattern captured by the camera with the wavelength emitted by the tunable laser. Speckle intensity data across various wavelengths are sent to a computer, which then constructs the TM for the spectral-encoding scatterer. After this calibration procedure, when employing the spectrometer, one simply needs to remove the tunable laser and couple the tested light into the system's input port. The schematic diagram of the experimental configuration is shown in Supplementary Section 5.

5.2 Neural network for spectrum reconstruction

The neural network used here is a CNN, which comprises three convolution blocks with filter numbers of 32, 16, and 8, respectively. All the filter sizes are 3 × 3 pixels, with a stride of 2 pixels. Each convolution layer is followed by a rectifier linear unit (ReLU) activation function layer. Following the convolution blocks, two fully connected layers with 1,001 neurons are present. The output vector is converted into a probability distribution across various wavelengths by applying the Softmax function. This transformation ensures that each element's value falls within the interval [0, 1], and the sum of all elements equals unity. We utilize the Root Mean Square Propagation optimizer with an initial learning rate of 2×10^{-4} to optimize the weights and biases. A learning rate attenuation coefficient of 0.99 is introduced at each epoch to enhance convergence. The input speckle image I in our study has 36×36 pixels, and the output spectrum S is 1,001×1. The pure data-driven neural network and DDNet training require about 15 hours to bring the loss function to ~2×10^{-6}, respectively. The method of early stopping is employed to conserve computational resources. Spectral reconstruction is performed in Matlab R2024a on standard computing hardware (2.1 GHz Intel Core i7 CPU and 16.0 GB RAM, without using GPUs).

5.3 Spectral reconstruction evaluation metrics

In this study, the relative L2-norm error (μ) is employed to quantify the reconstruction accuracy of the output spectra relative to the reference spectra. Denoting $S'\in\mathbb{R}^{M\times1}$ as the reconstructed spectrum, and $S\in\mathrm{R}^{M\times1}$ as the reference spectra, μ can be defined as:

$$\mu\left(S, S'\right) = \frac{\left\|S - S'\right\|_2}{\left\|S\right\|_2} . \tag{6}$$

Particularly, the *PSNR* is employed to assess the reconstruction quality of peak-shape spectra. Given *MAX* the maximum possible value of the spectra, the *PSNR* can be calculated as below:

$$MSE\left(S, S'\right) = \frac{1}{M}\sum_{m=1}^{M}\left[S'\left(\lambda_m\right) - S\left(\lambda_m\right)\right]^2 , \tag{7}$$

$$PSNR\left(S, S'\right) = 10 \cdot \log_{10}\left[\frac{MAX^2}{MSE\left(S, S'\right)}\right] . \tag{8}$$

References

1. Li A, Yao CH, Xia JF et al. Advances in cost-effective integrated spectrometers. *Light Sci Appl* **11**, 174 (2022).
2. Zhang YJ, Albrow-Owen T, Zhao ZY et al. Miniaturized disordered photonic molecule spectrometer. *Light Sci Appl* **14**, 144 (2025).
3. Zhang B, Wang Z, Albrow-Owen T et al. 3D ultra-broadband optically dispersive microregions in lithium niobate. *Nat Commun* **16**, 6086 (2025).
4. Zhang YR, Yang EB, Yoon HH et al. Reconstructive spectrometers: hardware miniaturization and computational reconstruction. *eLight* **5**, 23 (2025).
5. Lee DG, Song G, Lee C et al. Reconstructive spectrometer using double-layer disordered metasurfaces. *Sci Adv* **11**, eadv2376 (2025).
6. Cao H, Eliezer Y. Harnessing disorder for photonic device applications. *Appl Phys Rev* **9**, 011309 (2022).
7. Yang ZY, Albrow-Owen T, Cai WW et al. Miniaturization of optical spectrometers. *Science* **371**, eabe0722 (2021).
8. Gupta RK, Bruce GD, Powis SJ et al. Deep learning enabled laser speckle wavemeter with a high dynamic range. *Laser Photonics Rev* **14**, 2000120 (2020).
9. Metzger NK, Spesyvtsev R, Bruce GD et al. Harnessing speckle for a sub-femtometre resolved broadband wavemeter and laser stabilization. *Nat Commun* **8**, 15610 (2017).
10. Chen HZ, Duan ZY, Guan CY et al. A high resolution compact all-fiber spectrometer based on periodic refractive index modulation. *Appl Phys Lett* **122**, 231101 (2023).
11. Liang JR, Li J, Huang ZM et al. High-resolution miniaturized speckle spectrometry using fuse-induced fiber microvoids. *Photonics Res* **13**, 2654–2667 (2025).
12. Cao H, Čižmár T, Turtaev S et al. Controlling light propagation in multimode fibers for imaging, spectroscopy, and beyond. *Adv Opt Photonics* **15**, 524–612 (2023).
13. Kurekci S, Kahraman SS, Yuce E. Single-pixel multimode fiber spectrometer via wavefront shaping. *ACS Photonics* **10**, 2488–2493 (2023).
14. Liang JR, Li J, He JH et al. Multi-wavelength spectral reconstruction with localized speckle pattern. *Opt Commun* **575**, 131266 (2025).
15. Redding B, Popoff SM, Cao H. All-fiber spectrometer based on speckle pattern reconstruction. *Opt Express* **21**, 6584–6600 (2013).
16. Redding B, Popoff SM, Bromberg Y et al. Noise analysis of spectrometers based on speckle pattern reconstruction. *Appl Opt* **53**, 410–417 (2014).
17. Meng ZY, Li JQ, Yin CJ et al. Multimode fiber spectrometer with scalable bandwidth using space-division multiplexing. *AIP Adv* **9**, 015004 (2019).
18. Xu SB, Zhang JH, Cheng JW et al. Integrated spatial-temporal

random speckle spectrometer with high resolution in the C-band. *Photonics Res* **12**, 1556–1563 (2024).
19. Yoon HH, Fernandez HA, Nigmatulin F et al. Miniaturized spectrometers with a tunable van der Waals junction. *Science* **378**, 296–299 (2022).
20. Yang ZY, Albrow-Owen T, Cui HX et al. Single-nanowire spectrometers. *Science* **365**, 1017–1020 (2019).
21. Tua D, Liu RY, Yang WH et al. Imaging-based intelligent spectrometer on a plasmonic rainbow chip. *Nat Commun* **14**, 1902 (2023).
22. Yao CH, Xu KN, Zhang WL et al. Integrated reconstructive spectrometer with programmable photonic circuits. *Nat Commun* **14**, 6376 (2023).
23. Redding B, Liew SF, Sarma R et al. Compact spectrometer based on a disordered photonic chip. *Nat Photonics* **7**, 746–751 (2013).
24. French R, Gigan S, Muskens OL. Snapshot fiber spectral imaging using speckle correlations and compressive sensing. *Opt Express* **26**, 32302–32316 (2018).
25. Liew SF, Redding B, Choma MA et al. Broadband multimode fiber spectrometer. *Opt Lett* **41**, 2029–2032 (2016).
26. Feng F, Gan JA, Chen PF et al. AI-assisted spectrometer based on multi-mode optical fiber speckle patterns. *Opt Commun* **522**, 128675 (2022).
27. Cen QQ, Pian S, Liu XH et al. Microtaper leaky-mode spectrometer with picometer resolution. *eLight* **3**, 9 (2023).
28. Wang JJ, Zhang FY, Zhou XH et al. Miniaturized spectrometer based on MLP neural networks and a frosted glass encoder. *Opt Express* **32**, 30632–30641 (2024).
29. Wang TL, Tao JC, Wang X et al. Decoding wavelengths from compressed speckle patterns with deep learning. *Opt Lasers Eng* **180**, 108268 (2024).
30. Gao Z, Jiang T, Zhang MM et al. Breaking the speed limitation of wavemeter through spectra-space-time mapping. *Light Adv Manuf* **4**, 1 (2024).
31. Cai R, Xiao Y, Sui X et al. Compact wavemeter incorporating femtosecond laser-induced surface nanostructures enabled by deep learning. *Opt Lett* **48**, 3961–3964 (2023).
32. Sun YW, Ni FC, Huang YW et al. Near-infrared speckle wavemeter based on nonlinear frequency conversion. *Opt Lett* **48**, 4049–4052 (2023).
33. Shen CF, Pan TQ, Wei YH et al. Intelligent optical fiber-integrated near-infrared polarimeter based on upconversion nanoparticles. *Adv Opt Mater* **11**, 2301259 (2023).
34. Zhu SK, Zheng ZH, Meng WJ et al. Harnessing disordered photonics via multi-task learning towards intelligent four-dimensional light field sensors. *PhotoniX* **4**, 26 (2023).
35. Eversberg T, Vollmann K. Fundamentals of echelle spectroscopy. In Eversberg T, Vollmann K. *Spectroscopic Instrumentation: Fundamentals and Guidelines for Astronomers* 193–227 (Springer, Berlin, Heidelberg, 2015).
36. Bourdarot G, Le Coarer E, Bonfils X et al. NanoVipa: a miniaturized high-resolution echelle spectrometer, for the monitoring of young stars from a 6U Cubesat. *CEAS Space J* **9**, 411–419 (2017).
37. Le Coarer E, Blaize S, Benech P et al. Wavelength-scale stationary-wave integrated Fourier-transform spectrometry. *Nat Photonics* **1**, 473–478 (2007).
38. Sugavanam S, Sorokina M, Churkin DV. Spectral correlations in a random distributed feedback fibre laser. *Nat Commun* **8**, 15514 (2017).
39. Wang F, Bian YM, Wang HC et al. Phase imaging with an untrained neural network. *Light Sci Appl* **9**, 77 (2020).
40. Wang F, Wang CL, Chen ML et al. Far-field super-resolution ghost imaging with a deep neural network constraint. *Light Sci Appl* **11**, 1 (2022).
41. Wan YY, Fan XY, Xu BX et al. Reconstructive spectrum analyzer with high-resolution and large-bandwidth using physical-model and data-driven model combined neural network. *Laser Photonics Rev* **17**, 2201018 (2023).
42. Lempitsky V, Vedaldi A, Ulyanov D. Deep image prior. In *2018 IEEE/CVF Conference on Computer Vision and Pattern Recognition* 9446–9454 (IEEE, 2018). http://doi.org/10.1109/CVPR.2018.00984.
43. Qayyum A, Ilahi I, Shamshad F et al. Untrained neural network priors for inverse imaging problems: a survey. *IEEE Trans Pattern Anal Mach Intell* **45**, 6511–6536 (2023).
44. Wang KQ, Song L, Wang CT et al. On the use of deep learning for phase recovery. *Light Sci Appl* **13**, 4 (2024).
45. Bai C, Peng T, Min JW et al. Dual-wavelength in-line digital holography with untrained deep neural networks. *Photonics Res* **9**, 2501–2510 (2021).
46. Liu KX, Wu JC, He ZH et al. 4K-DMDNet: diffraction model-driven network for 4K computer-generated holography. *Opto-Electron Adv* **6**, 220135 (2023).
47. Huang ZZ, Cao LC. Quantitative phase imaging based on holography: trends and new perspectives. *Light Sci Appl* **13**, 145 (2024).
48. Li RJ, Pedrini G, Huang ZZ et al. Physics-enhanced neural network for phase retrieval from two diffraction patterns. *Opt Express* **30**, 32680–32692 (2022).
49. Chen Q, Huang DL, Chen R. Fourier ptychographic microscopy with untrained deep neural network priors. *Opt Express* **30**, 39597–39612 (2022).
50. He Y, Yao YH, He YL et al. Untrained neural network enhances the resolution of structured illumination microscopy under strong background and noise levels. *Adv Photonics Nexus* **2**, 046005 (2023).
51. Jin YB, Lu LP, Zhou S et al. Neural-field-assisted transport-of-intensity phase microscopy: partially coherent quantitative phase imaging under unknown defocus distance. *Photonics Res* **12**, 1494–1501 (2024).
52. Huang LQ, Luo RC, Liu X et al. Spectral imaging with deep learning. *Light Sci Appl* **11**, 61 (2022).
53. Tu HS, Liu HT, Pan TQ et al. Deep empirical neural network for optical phase retrieval over a scattering medium. *Nat Commun* **16**, 1369 (2025).
54. Huang LZ, Chen HL, Liu TR et al. Self-supervised learning of hologram reconstruction using physics consistency. *Nat Mach Intell* **5**, 895–907 (2023).
55. Coluccelli N, Cassinerio M, Redding B et al. The optical frequency comb fibre spectrometer. *Nat Commun* **7**, 12995 (2016).
56. Redding B, Liew SF, Bromberg Y et al. Evanescently coupled multimode spiral spectrometer. *Optica* **3**, 956–962 (2016).
57. Zhang ZM, Xiao SM, Song QH et al. Scalable on-chip diffractive speckle spectrometer with high spectral channel density. *Light Sci Appl* **14**, 130 (2025).
58. Shi ZL, Mettes P, Maji S et al. On measuring and controlling the spectral bias of the deep image prior. *Int J Comput Vis* **130**, 885–908 (2022).
59. Liu YL, Pang YK, Li J et al. Architecture-agnostic untrained network priors for image reconstruction with frequency regularization. *In 18th European Conference on Computer Vision* 341–358 (Springer, 2024). http://doi.org/10.1007/978-3-031-72630-9_20.
60. Chakrabarty P, Maji S. The spectral bias of the deep image prior. arXiv preprint arXiv: 1912.08905, 2019. https://doi.org/10.48550/arXiv.1912.08905
61. Darweesh R, Yadav RK, Adler E et al. Nonlinear self-calibrated spectrometer with single GeSe-InSe heterojunction device. *Sci Adv* **10**, eadn6028 (2024).
62. Yang T, Peng JX, Li XA et al. Compact broadband spectrometer based on upconversion and downconversion luminescence. *Opt Lett* **42**, 4375–4378 (2017).
63. Liang JR, Ye J, Ke YZ et al. Polarization transmission matrix

enabled high-accuracy, large-bandwidth speckle-based reconstructive spectrometer. *Appl Phys Lett* **124**, 071111 (2024).
64. Dainty JC. *Laser Speckle and Related Phenomena* (Springer, Berlin, Heidelberg, 1975).
65. Xu HN, Qin Y, Hu GL et al. Integrated single-resonator spectrometer beyond the free-spectral-range limit. *ACS Photonics* **10**, 654–666 (2023).
66. Sun CL, Chen ZQ, Ye YT et al. Scalable on-chip microdisk resonator spectrometer. *Laser Photonics Rev* **17**, 2200792 (2023).
67. Xu HN, Qin Y, Hu GL et al. Cavity-enhanced scalable integrated temporal random-speckle spectrometry. *Optica* **10**, 1177–1188 (2023).
68. Wan NH, Meng F, Schröder T et al. High-resolution optical spectroscopy using multimode interference in a compact tapered fibre. *Nat Commun* **6**, 7762 (2015).
69. Li A, Wang C, Bao FX et al. An integrated single-shot spectrometer with large bandwidth-resolution ratio and wide operation temperature range. *PhotoniX* **4**, 29 (2023).
70. Fan YD, Huang WA, Zhu F et al. Dispersion-assisted high-dimensional photodetector. *Nature* **630**, 77–83 (2024).
71. Zheng ZH, Zhu SK, Chen Y et al. Towards integrated mode-division demultiplexing spectrometer by deep learning. *Opto-Electron Sci* **1**, 220012 (2022).
72. Du XC, Wang Y, Cui Y et al. A microspectrometer with dual-signal spectral reconstruction. *Nat Electron* **7**, 984–990 (2024).
73. Mondal A, Debnath K. Design of resolution-tunable neural network-based integrated reconstructive spectrometer. *IEEE Sens J* **22**, 2630–2636 (2022).
74. Wang JY, Pan BB, Wang Z et al. Single-pixel p-graded-n junction spectrometers. *Nat Commun* **15**, 1773 (2024).
75. Zhang WY, Song HY, He X et al. Deeply learned broadband encoding stochastic hyperspectral imaging. *Light Sci Appl* **10**, 108 (2021).
76. Li X, Wang J, Yu FL et al. Nonlinear memristive computational spectrometer. *Light Sci Appl* **14**, 47 (2025).
77. Wen JR, Hao LY, Gao C et al. Deep learning-based miniaturized all-dielectric ultracompact film spectrometer. *ACS Photonics* **10**, 225–233 (2023).
78. Zhou J, Zhang H, Qiao QF et al. Denoising-autoencoder-facilitated MEMS computational spectrometer with enhanced resolution on a silicon photonic chip. *Nat Commun* **15**, 10260 (2024).
79. Yi D, Tsang HK. High-resolution and broadband two-stage speckle spectrometer. *J Lightwave Technol* **40**, 7969–7976 (2022).
80. Tang PS, Zheng KP, Yuan WM et al. Learning to transmit images through optical speckle of a multimode fiber with high fidelity. *Appl Phys Lett* **121**, 081107 (2022).
81. Caramazza P, Moran O, Murray-Smith R et al. Transmission of natural scene images through a multimode fibre. *Nat Commun* **10**, 2029 (2019).
82. Xu HN, Qin Y, Hu GL et al. Breaking the resolution-bandwidth limit of chip-scale spectrometry by harnessing a dispersion-engineered photonic molecule. *Light Sci Appl* **12**, 64 (2023).
83. Yao CH, Zhang WL, Bao P et al. Chip-scale sensor for spectroscopic metrology. *Nat Commun* **15**, 10305 (2024).
84. Tian MH, Liu BL, Lu ZL et al. Miniaturized on-chip spectrometer enabled by electrochromic modulation. *Light Sci Appl* **13**, 278 (2024).
85. Wen S, Xue XY, Wang S et al. Metasurface array for single-shot spectroscopic ellipsometry. *Light Sci Appl* **13**, 88 (2024).
86. Wen Z, Dong ZY, Deng QL et al. Single multimode fibre for in vivo light-field-encoded endoscopic imaging. *Nat Photonics* **17**, 679–687 (2023).

Acknowledgements

We are grateful for financial supports from the National Natural Science Foundation of China (NSFC) (62305385, 62305391), National University of Defense Technology Research Fund Project (22-061, 2024-ZZCX-BC-03, ZK2023-60).

Author contributions

All authors commented on the manuscript. J. R. Liang carried out the research work, developed architecture and performed the data analysis. M. Jiang proposed the concept and debugged the code. J. Li, J.M. Xu, and P. Zhou conceived the research framework. Z. M. Huang, J. H. He, and Y.T. Guo assisted in conducting the experiments. J. Ye and J. Y. Leng provided constructive suggestions and feedback. The text was written by J. R. Liang, M. Jiang, J. Li, J. M. Xu and P. Zhou.

Competing interests

The authors declare that there are no conflicts of interest related to this article.

Supplementary information

Supplementary information for this paper is available at https://doi.org/10.29026/oea.2026.250299

Published by Editorial Office of *Opto-Electronic Advance*, Institute of Optics and Electronics, Chinese Academy of Sciences.